Journal of Colloid and Interface Science 647 (2023) 331–343

Contents lists available at ScienceDirect

Journal of Colloid And Interface Science

journal homepage: www.elsevier.com/locate/jcis

Regular Article

Pore-scale Ostwald ripening of gas bubbles in the presence of oil and water in porous media

Deepak Singh [a,*], Helmer André Friis [a], Espen Jettestuen [b], Johan Olav Helland [c]

[a] Department of Energy and Petroleum Engineering, University of Stavanger, P.O. Box 8600, N-4036 Stavanger, Norway
[b] NORCE Norwegian Research Centre, Tullins gate 2, N-0166 Oslo, Norway
[c] NORCE Norwegian Research Centre, P.O. Box 8046, N-4068 Stavanger, Norway

ARTICLE INFO

Dataset link: https://doi.org/10.6084/m9.figshare.21836859.v1

Keywords:
Ostwald ripening
Three-phase
Pore-scale
Level set method

ABSTRACT

Hypothesis: Ostwald ripening of gas bubbles is a spontaneous mass transfer process that can impact the storage volume of trapped gas in the subsurface. In homogeneous porous media with identical pores, bubbles evolve toward an equilibrium state of equal pressure and volume. How the presence of two liquids impacts ripening of a bubble population is less known. We hypothesize that the equilibrium bubble sizes depend on the surrounding liquid configuration and oil/water capillary pressure.

Method and numerical experiments: We investigate ripening of nitrogen bubbles in homogeneous porous media containing decane and water using a level set method that alternately simulates capillary-controlled displacement and mass transfer between bubbles to eradicate chemical-potential differences. We explore impacts of initial fluid distribution and oil/water capillary pressure on the bubble evolution.

Findings: Ripening in three-phase scenarios in porous media stabilizes gas bubbles to sizes that depend on their surrounding liquids. Bubbles in oil decrease in size while bubbles in water increase in size with increasing oil/water capillary pressure. Bubbles in oil reach local equilibrium before the three-phase system stabilizes globally. A potential implication for field-scale gas storage is that the trapped gas fractions in oil and water vary with depth in the oil/water transition zone.

1. Introduction

Subsurface gas storage technologies play an important role in the transition toward cleaner energy production [1]. Permanent storage of carbon dioxide (CO_2) is a means to limit emissions to the atmosphere and restrain global warming [2], while underground storage of hydrogen and natural gases like methane are means to store energy in the short term for subsequent recovery and use [3–5]. Common to both of these applications is the occurrence of residual gas trapping in the reservoir: After gas has been injected into the porous rock, brine imbibes into the pore space occupied by the migrating gas plume and disconnects gas ganglia that get trapped by capillary forces. Such residual trapping is a mechanism for storing significant amounts of CO_2 [6–10], but for temporary storage this is a disadvantage as trapped gas is hard to recover later [4,5]. Reuse of depleted hydrocarbon reservoirs for storage leads to trapped gas ganglia in the presence of both oil and water. This is an attractive option because these reservoirs have existing infrastructure, known geology, and well-studied rock material from the oil production phase, while geological traps occupying oil are considered safe storage locations [11,12]. Three-phase flow experiments on water-wet core samples also show enhanced gas trapping in the presence of oil and water compared with two-phase gas/water systems [13,14], although the results depend on the displacement history of oil and water before the scheduled gas/water injection cycle [15].

A comprehensive body of works has investigated two-phase residual trapping in porous rock to understand impacts of initial saturation, process history, flow rate, wetting state, porous material and length scale [3,7–10,16–20]. However, mass transfers between phases may alter capillary trapped fluid configurations further after imbibition. In particular, trapped gas ganglia do not remain stagnant but rather evolve over time through diffusive mass transfers toward thermodynamic equilibrium at which the gas chemical potential (or pressure) is constant in time and space [21–27]. This process of coarsening and anti-coarsening is called Ostwald ripening, and it is affected by fluid properties, fluid-solid interactions, pore geometry, and length scales [23,25,26]. Ostwald ripening of residual gas bubble distributions has been investigated at

* Corresponding author.
E-mail address: deepak.singh@uis.no (D. Singh).

https://doi.org/10.1016/j.jcis.2023.05.070
Received 14 March 2023; Received in revised form 3 May 2023; Accepted 11 May 2023
Available online 25 May 2023

pore scale in two-phase systems [e.g., 22,25,26,28]. Despite the opportunity of enhanced gas trapping in three-phase systems, it is less known how mass transfers between gas ganglia will alter residual three-phase configurations in porous rock over time. In this work we initiate investigations of this matter using a numerical model for simulating Ostwald ripening of gas bubbles in the presence of oil and water in porous media.

Ostwald ripening is a slow diffusion process with vastly different time scales at pore scale and field scale. Blunt [21] carried out theoretical field-scale analysis of ripening in a 100 m thick reservoir of trapped gas and concluded that the time scale for equilibrium and subsequent formation of mobile gas regions is in the range of 10^6 years. A similar analysis performed by Xu et al. [27] on ripening due to buoyant forces yielded a time scale of 10^4 years to form a 3 m thick gas cap. However, theoretical [21], numerical [22] and experimental [26] studies have shown that the equilibration occurs within a matter of days at the pore scale (albeit strongly depending on gas type [21,25]). Analysis of imaged pore-scale gas/water distributions from two-phase experiments in porous rock shows large spatial capillary pressure variation of gas ganglia, demonstrating high potential for ripening [29,30]. As mass transfer typically decreases exponentially with time, the most significant impacts of ripening might happen much earlier than at the time of thermodynamic equilibrium [e.g., 22,25,26]. Growth or shrinkage of gas ganglia may also lead to capillary instabilities that could trigger displacement [22,25].

Microtomography imaging of fluid configurations in porous rock shows that the mechanisms for enhanced oil recovery during three-phase flow are slow drainage through thin continuous oil layers surrounded by gas and water as well as double displacements where gas displaces oil ganglia that displaces water [31–34]. Enhanced gas trapping occurs when oil snaps off gas and form gas ganglia during reversed double displacements where water displaces oil that displaces gas [32–35]. The extent to which trapped gas directly contacts either oil, water or both liquids depend on the wetting order of the fluids, the ability of oil to spread on the gas/water interface (i.e., the spreading coefficient), and the displacement history [32–36]. Significant gas trapping is associated with high gas/liquid interfacial area and three-phase configurations also show large variation of gas ganglia capillary pressures [37,38], both of which facilitate mass transfer. Still, the impact of Ostwald ripening on the storage life of three-phase residual gas configurations in porous rock has not been the subject of research investigations thus far.

A typical numerical model for ripening of gas-bubble distributions will simulate two processes: interface readjustment and diffusive mass transfer through the intermediate liquid phase. Here, it is convenient to model them in alternate steps, with the mass transfer step being the rate-determining process [22]. The interface readjustment step calculates gas-bubble pressures and interface locations for updated bubble volumes as a response to mass exchanges in the pore geometry. One way to model this feature is by taking predetermined pressure-volume relationships for the pertinent geometry as input to the simulation. This approach has been used for two-phase configurations in pore-network models with idealized pore geometry [22,28]. However, for three fluid phases such an approach is less applicable as the shape, pressure, and interface locations of a gas bubble depend on the surrounding oil/water configuration. Another method is to calculate the gas-bubble pressures and interface locations for target bubble volumes by direct numerical simulation and then use these pressures to determine future mass transfers [25]. The multiphase level set (MLS) method [39,40] serves this purpose as it simulates capillary equilibrium states in complex pore geometries for two-phase and three-phase fluid systems with prescribed fluid pressures or fluid volumes.

Mass transfers during the ripening of gas-bubble distributions typically decrease exponentially with time [25,26], so it is prudent to use adaptive time steps to make simulations computationally efficient [22,28]. Determining suitable adaptive time steps is challenging in real pore geometries since grid resolution and discretization of a continuous mass transfer with large time steps can lead to mass transfer cyclicity. This means that a discrete amount of mass transferred from one bubble to another will be transferred in the reversed direction the next time step [25]. Hence, time steps have to be chosen heuristically and within suitable ranges. Another issue with using large time steps is that they can omit details from the evolution (for example, local energy minima and capillary instabilities). Handling these problems is challenging in a two-phase pore-scale numerical investigation of ripening in porous media. They become even more complicated for ripening in a three-phase scenario since the time scale for gas diffusion through oil generally is different than for gas diffusion through the water.

This work investigates pore-scale Ostwald ripening of gas-bubble distributions surrounded by both oil and water in porous media. Experimental investigations show that in a kinetic environment with gas injection and gas bubble nucleation, convective transport diminishes the impact of ripening [41]. Herein, we consider stationary fluid configurations with capillary trapped gas to replicate storage scenarios after the fluid flow has ceased. We begin by stating the conditions for thermodynamic equilibrium in a three-phase configuration in porous media, and then we derive analytic expressions to investigate the possibility of three-phase equilibrium of gas bubbles in oil and water in the absence of a solid phase (section 2). To investigate the behaviour in porous media, we use a coupled numerical model based on the MLS method [39,40] that alternately simulates capillary-controlled displacement toward equilibrium and mass transfer between bubbles governed by differences in chemical potential of the gas component (section 3). The mass transfer between gas bubbles accounts for all effective gas diffusion paths through oil and water and across oil/water interfaces. We perform three-phase simulations on a 2D homogeneous pore geometry where all pores are identical (section 4). Ripening of two-phase gas/water configurations in such geometries have shown that gas bubbles equilibrate to a unique bubble size and pressure irrespective of initial configuration when gas bubbles occupy single pores [26,28]. We replicate this behaviour with two-phase simulations, and then we perform three-phase simulations to show that in the latter configurations, the bubble sizes at equilibrium depend on whether they contact oil, water, or both liquids. Further simulations show that this behaviour is a function of the prevailing oil/water capillary pressure. Analytic calculations of equilibrium gas bubble volumes surrounded by oil and water confirm the simulated results. Finally, section 5 provides the conclusions and suggests scope for future work.

2. Three-phase equilibrium

We consider a closed system that consists of a static porous medium with solid grains (s) and pore space saturated with partially miscible gas (g), oil (o), and water (w). We assume the system is isothermal, and the gas phase is compressible (which has minor impact at reservoir pressure) while oil and water are incompressible. Then, for a system where volume and amount of material components are constant, thermodynamic equilibrium occurs when the Helmholtz free energy F is at a minimum [42]. The change in Helmholtz energy is:

$$dF = -\sum_{\alpha=g,o,w} P_\alpha dV_\alpha + \sum_{\alpha\beta=go,ow,gw,gs,os,ws} \sigma_{\alpha\beta} dA_{\alpha\beta} + \sum_{\alpha=g,o,w}\sum_i \mu_{i,\alpha} dN_{i,\alpha} + \sum_{\alpha\beta=go,ow,gw}\sum_i \mu_{i,\alpha\beta} dN_{i,\alpha\beta}. \quad (1)$$

Here, P_α [Pa] and V_α [m^3] are phase pressure and volume, while $\sigma_{\alpha\beta}$ [Nm^{-1}] and $A_{\alpha\beta}$ [m^2] are interfacial tension and interface area, respectively. The number of molecules of component i in fluid phase α and on fluid/fluid interfaces $\alpha\beta$ is $N_{i,\alpha}$ and $N_{i,\alpha\beta}$, respectively. The corresponding chemical potentials are $\mu_{i,\alpha}$ and $\mu_{i,\alpha\beta}$. We will further assume the system contains one gas component and that this is the only component that can be transferred across interfaces; hence we omit subscript i on μ and N. Further, in equation (1) we do not consider compositional

changes along solid/fluid interfaces, so we assume the wetting state of the solid is static.

The change in fluid phase volumes, fluid/solid interfacial areas, and the amount of gas molecules satisfy the following relations:

$$\sum_{\alpha=g,o,w} dV_\alpha = 0, \quad \sum_{\alpha\beta=gs,os,ws} dA_{\alpha\beta} = 0,$$
$$\sum_{\alpha=g,o,w} dN_\alpha + \sum_{\alpha\beta=go,ow,gw} dN_{\alpha\beta} = 0. \tag{2}$$

At this stage we also introduce capillary pressure $P_{\alpha\beta}$ and the Young-Laplace equation:

$$P_{\alpha\beta} = P_\alpha - P_\beta = \sigma_{\alpha\beta} C_{\alpha\beta}, \ \alpha\beta = go, ow, gw, \tag{3}$$

where C [m^{-1}] is interface curvature. The contact angle $\theta_{\alpha\beta}$ is the angle measured through the denser fluid phase β between the tangential planes of the solid surface and the $\alpha\beta$ fluid/fluid interface at the $\alpha\beta s$ contact line. Young's equation relates the contact angle to the interfacial tensions:

$$\sigma_{\alpha\beta}\cos\theta_{\alpha\beta} = \sigma_{\alpha s} - \sigma_{\beta s}, \ \alpha\beta = go, ow, gw. \tag{4}$$

In a three-phase system it follows from equation (3) that the capillary pressures are related by $P_{gw} = P_{go} + P_{ow}$. Similarly, equation (4) implies that the three-phase contact angles and interfacial tensions satisfy the Bartell-Osterhof equation [e.g., 43]:

$$\sigma_{gw}\cos\theta_{gw} = \sigma_{go}\cos\theta_{go} + \sigma_{ow}\cos\theta_{ow}. \tag{5}$$

Thus, by combining equations (1)-(5), the two conditions that must be satisfied in thermodynamic equilibrium ($dF = 0$) are:

$$P_{ow}dV_w - P_{go}dV_g = \sigma_{ow}\cos\theta_{ow}dA_{ws}$$
$$-\sigma_{go}\cos\theta_{go}dA_{gs} - \sum_{\alpha\beta=go,ow,gw} \sigma_{\alpha\beta}dA_{\alpha\beta}, \tag{6}$$

and

$$\mu = \mu_\alpha = \mu_\beta = \mu_{\alpha\beta}, \ \alpha\beta = go, ow, gw. \tag{7}$$

Equation (6) holds for capillary equilibrium and it has previously been used to calculate three-phase capillary entry pressures in pore throats [44–46]. The second condition, equation (7), states that the chemical potential of the gas component, and hence the partial gas pressure, is equal in all fluid phases.

Ostwald ripening of gas bubbles is a spontaneous inter-bubble diffusive mass transfer process, governed by the gas concentration gradient in the liquid, by which low-pressure bubbles consume high-pressure bubbles to minimize Gibbs free energy [47]. In thermodynamic equilibrium the gas bubble pressures (and the chemical potentials) must become equal. The mass transfer occurs through a liquid phase ($l = o, w$) in which the gas phase (g) is soluble and the concentration of the gas in the surrounding liquid is given by Henry's law:

$$\frac{n_g}{n_l} \approx \frac{P_g}{K_l^{px}} = \frac{(P_l + P_{gl})}{K_l^{px}}, \tag{8}$$

where n_g [mol] is the number of moles of gas in n_l moles of liquid and K_l^{px} [Pa] is Henry's volatility in liquid l.

2.1. Bulk fluid scenario

Here we examine a 2D space filled with oil, water, and two gas bubbles: Bubble 1 is surrounded by water, and bubble 2 is surrounded by oil (see Fig. 1). Our objective is to analyse whether such a configuration is in thermodynamic equilibrium after Ostwald ripening. The Young-Laplace equation relates the capillary pressure between gas and the surrounding liquid to the bubble interfacial radius:

$$P_{gw} = \frac{\sigma_{gw}}{R_{g1}} \quad \text{and} \quad P_{go} = \frac{\sigma_{go}}{R_{g2}}, \tag{9}$$

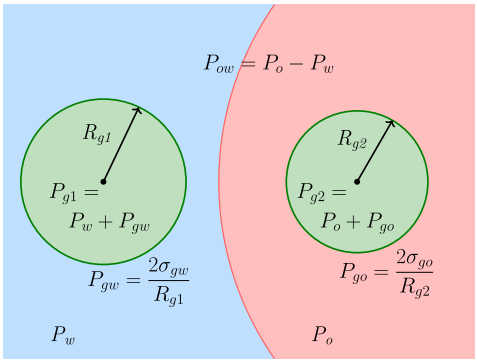

Fig. 1. Gas bubbles (*green*) surrounded by oil (*red*) and water (*blue*) in the absence of a solid phase.

where R_{g1} and R_{g2} [m] are the radii of the gas bubbles surrounded by water and oil, respectively. From equation (3) and (9) we get:

$$P_{g1} - P_{g2} = \frac{\sigma_{gw}}{R_{g1}} - \frac{\sigma_{go}}{R_{g2}} - P_{ow} = \Delta P. \tag{10}$$

In a state of thermodynamic equilibrium the two bubbles should have equal pressures (i.e., $\Delta P = 0$), which reduces equation (10) to:

$$P_{ow} = \frac{\sigma_{gw}}{R_{g1,eq}} - \frac{\sigma_{go}}{R_{g2,eq}}. \tag{11}$$

We rearrange equation (11) to formulate relationships between the two bubble radii:

$$R_{g2,eq} = \frac{\sigma_{go} R_{g1,eq}}{\sigma_{gw} - P_{ow} R_{g1,eq}}. \tag{12}$$

In the special case $P_{ow} = 0$, equation (12) reduces to a linear relationship which states that the ratio of the gas-bubble radii is constant and equal to the ratio of the two gas/liquid interfacial tensions. For most multiphase fluid systems $\sigma_{gw} > \sigma_{go}$, implying that the larger bubble resides in water and the smaller bubble resides in oil at such a potential equilibrium state.

In the general case with non-zero P_{ow}, equation (12) shows that the bubble radii follow a hyperbola with vertical asymptote at $R_{g1,eq} = \sigma_{gw}/P_{ow}$ and horizontal asymptote at $R_{g2,eq} = -\sigma_{go}/P_{ow}$. However, the radius of the oil/water interface restricts the permissible range of bubble radii further. When $P_{ow} > 0$, there is a radius interval below a critical value $R_{g,crit}$ where the bubble size is still smaller in oil than in water. Fig. 2 provides a graphical illustration of this for given interfacial tensions and P_{ow}. Due to the hyperbolic nature of equation (12) this bubble-size difference diminishes as $R_{g1,eq}$ increases. Equation (11) shows that the two bubbles become equal in size when $R_{g,crit} = (\sigma_{gw} - \sigma_{go})/P_{ow} = (C_s + \sigma_{ow})/P_{ow}$, where we have introduced the oil spreading coefficient $C_s = \sigma_{gw} - \sigma_{go} - \sigma_{ow}$. For bubble radii above $R_{g,crit}$, the three-phase system essentially reduces to a two-phase gas/water system where the two bubbles have equal radii. For spreading oils ($C_s = 0$), a thin molecular oil film will then coat the gas bubbles so that the two bubble radii are equal to the radius of the oil/water interface, while for non-spreading oils ($C_s < 0$) the oil film ruptures and small oil droplets form on the gas/water interface instead.

For $P_{ow} < 0$, the bubble in water is also larger than the bubble in oil, see Fig. 2. However, for a sufficiently large $R_{g1,eq}$ the water layer breaks, and oil will surround both bubbles completely while the water, due to its strong non-spreading behaviour, forms droplets in the oil. At this stage, we have essentially a two-phase gas/oil scenario where the larger bubble 1 has a lower gas pressure than bubble 2, triggering mass transfer from bubble 2 to bubble 1. Eventually, bubble 2 has dissolved completely, while the size of bubble 1 has increased correspondingly.

This analysis shows that if an equilibrium state exists in which the two bubbles can coexist in a bulk three-phase system, the bubble in water will be larger than the bubble in oil. However, this is an unstable

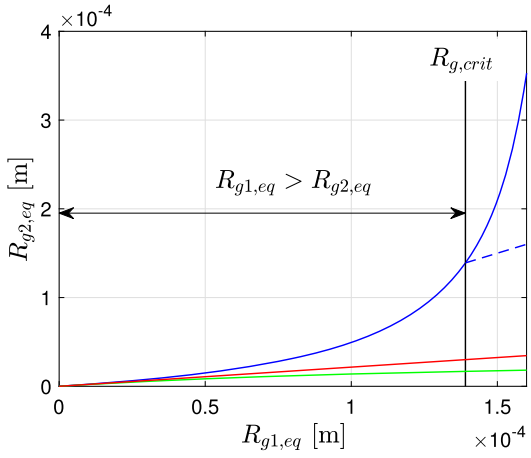

Fig. 2. Relationships between bubble radii for a potential coexistence of a gas bubble in oil and a gas bubble in water according to equation (12) for P_{ow} = 300 Pa (*blue*), $P_{ow} = 0$ Pa (*red*), and $P_{ow} = -300$ Pa (*green*). For $P_{ow} = 300$ Pa, we highlight the critical radius $R_{g,crit}$ (*vertical, solid line*): To the left of $R_{g,crit}$, $R_{g1,eq} > R_{g2,eq}$ (*blue, solid line*), while to the right of $R_{g,crit}$ a two-phase gas/water scenario occurs with $R_{g1,eq} = R_{g2,eq}$ (*dashed, blue line*). The interfacial tensions are $\sigma_{gw} = 53.22 \times 10^{-3}$ Nm^{-1} [48], $\sigma_{go} = 11.5 \times 10^{-3}$ Nm^{-1} [49], and $\sigma_{ow} = 43.65 \times 10^{-3}$ Nm^{-1} [50], representing a nitrogen-decane-water fluid system.

state. A small perturbation of the bubble radii away from the radius curve given by equation (12) leads to unequal bubble pressures, i.e., $\Delta P \neq 0$ in equation (10), which will trigger a feedback loop of mass transfer that leads to loss of one of the bubbles. For example, the addition of a small mass to bubble 1, so that $R_{g1} > R_{g1,eq}$ and $\Delta P < 0$, will trigger mass transfer from bubble 2 to bubble 1. This mass transfer will reduce R_{g2} and increase R_{g1} until the bubble in oil vanishes. Similarly, if we instead add a small mass to bubble 2 so that $R_{g2} > R_{g2,eq}$ and $\Delta P > 0$, then mass transfers from bubble 1 to bubble 2 which results in loss of the bubble in water. Thus, we conclude that for a thermodynamic equilibrium state achieved after ripening, the gas resides in only one of the liquids. This situation is analogous to a two-phase system in which a gas bubble distribution in a liquid coarsens due to unequal bubble pressures until one large bubble remains [e.g., 25].

The three-phase situation becomes more complex when both liquids contain more than one bubble. Then the coarsening is a collective result of simultaneous diffusive mass transfers between bubbles in the same liquid and between bubbles in oil and water. The time scales of these processes will have an impact on which liquid the gas will stabilize within in the final equilibrium state.

We have demonstrated that gas-bubble coarsening in a bulk three-phase system can transfer the gas spontaneously to either oil or water. The situation is more complex in porous media because narrow pore throats create energy barriers that will alter this monotonic coarsening. Gas bubbles inside pore geometries yield more complex pressure-volume behaviour that also depend on the wetting state and the surrounding oil/water configuration. Hence for porous media we anticipate that the coexistence of gas bubbles in oil and water persists after ripening. Such investigations require a numerical pore-scale model which we present in the next section.

3. Methods

3.1. Mass transfer approach

The model for ripening of residual gas bubbles in the presence of oil and water in porous media relies on the following assumptions: (i) The diffusive mass transfer is the rate-determining process, while the interface readjustment occurs instantaneously [22]; (ii) a liquid ganglion (or region) in contact with only one gas bubble is in thermodynamic equilibrium with it [42]; (iii) the mass transfer between gas bubbles occurs only through bulk liquid regions and due to chemical-potential differences across the liquid region boundary; (iv) two gas bubbles interact with each other only through the liquids [22]; (v) there is no mass accumulation or loss (dissolution) from gas bubbles to the intermediate liquid phases during Ostwald ripening – they only act as mass transfer paths between the bubbles; total gas volume is constant, with no flow and no gravity effect (due to small length scales) [26]; and (vii) reservoir temperature is above the critical temperature of the gas. The last assumption simplifies calculations by ensuring that the chemical species is in one phase, i.e., gas or supercritical fluid, and phase change calculations are not required.

Based on these assumptions, at constant pressure and temperature, the mass transfer rate for a diffusion path k in liquid l from a bubble j to another bubble i due to Ostwald ripening is [25]:

$$\frac{\partial n_{i,k}}{\partial t} = -J_l A_k \Delta\mu_{i,j} = -J_l A_k \times (RT)\left(\ln \frac{f_i}{f_j}\right). \tag{13}$$

Here, $\partial n_{i,k}/\partial t$ [mol s^{-1}] is the mole transfer rate through the diffusive transfer path k, J_l [mol^2 s kg^{-1} m^{-4}] is the effective phase permeability constant for mass transfer through liquid l, A_k [m^2] is the surface area through which the mass transfer occurs, $\Delta\mu_{i,j}$ is the chemical potential difference between the gas bubbles i and j, R [8.314 J mol^{-1} K^{-1}] is the universal gas constant, and f is the fugacity of gas in the bubble. The negative sign in equation (13) indicates mass transfer direction from higher potential to lower potential. For ideal gases, the chemical potential difference can be obtained by replacing fugacity by the bubble pressure P [42].

The effective phase permeability J_l can be found from Fick's first law of diffusion and Henry's law as [26]:

$$J_l \approx \left(\frac{\rho_l M_g}{Z \rho_g M_l {V_m}^2} \times \frac{D_l}{K_l^{px}} \times \frac{1}{\bar{l}}\right), \tag{14}$$

where M_α [kg mol^{-1}] and ρ_α [kg m^{-3}] are the molecular weight and density of phase α, Z is the gas compressibility factor, V_m [m^3 mol^{-1}] is the molar volume of gas, D_l [m^2 s^{-1}] is the diffusion coefficient of gas in liquid l, and $\bar{l}$ [m] is the effective mass transfer distance between a specific bubble and its neighbour. Equation (14) differs slightly from the expression presented by Xu et al. [26] as we model mass transfer governed by differences in chemical potentials rather than pressures. In case of real gases, we calculate the fugacity of gas bubbles in equation (13) and gas compressibility factor in equation (14) using Peng-Robinson equation of state. Typically reservoir pressure is several orders of magnitude larger than the local gas/liquid capillary pressure variations. Singh et al. [25] showed that these variations have a negligible impact on the calculation of the compressibility factor. Hence, in this work, we use the reservoir pressure to calculate a common gas compressibility factor for all the gas bubbles.

In our model, we simulate the Ostwald ripening as alternate steps of constant-pressure diffusive mass transfer followed by fluid/fluid interface readjustment (see Singh et al. [25] for details and flowchart of two-phase simulations). The mass transfer step aims at eliminating chemical potential differences between gas bubbles (equation (7)), while the interface readjustment step evolves the interfaces to maintain capillary equilibrium (equation (6)). The latter step uses the MLS method [39,40] which calculates the interface positions as well as the pressures, volumes and surface areas of the gas bubbles during the ripening process.

3.2. Multiphase level set method for capillary-controlled displacement

The MLS method uses one level set function ϕ_α for each fluid phase α. These functions describe signed distances to the phase boundaries, such that $\phi_\alpha < 0$ inside phase α, $\phi_\alpha > 0$ on the outside, and $\phi_\alpha = 0$ on the phase boundaries. Similarly, a static level set function ψ describes the pore geometry with respect to pore walls ($\psi = 0$), solid space ($\psi < 0$) and pore space ($\psi > 0$). To each fluid phase we also assign a surface

tension γ_α and a solid/fluid intersection angle ζ_α which is measured through phase α and used to form contact angles on the pore walls. These are related to the fluid/fluid interfacial tensions $\sigma_{\alpha\beta}$ and contact angles $\theta_{\alpha\beta}$ by the following relations [39]:

$$\begin{aligned} &\sigma_{\alpha\beta} = \gamma_\alpha + \gamma_\beta \ , \\ &\cos\theta_{\alpha\beta} = \frac{\gamma_\beta \cos\zeta_\beta - \gamma_\alpha \cos\zeta_\alpha}{\gamma_\beta + \gamma_\alpha} . \end{aligned} \tag{15}$$

Here we follow Helland et al. [39] and set $\zeta_w = \theta_{ow}$, $\zeta_o = 180° - \theta_{ow}$, $\zeta_g = 180°$, consistent with equation (5).

The evolution equations for the fluid level set functions ϕ_α use a Heaviside step function H that separates the velocity term for capillary-controlled fluid displacement in the pore space and the velocity term for contact angle formation on the pore walls (which is extended into the solid space for increased accuracy) [39,40]:

$$\begin{aligned} &\frac{\partial\phi_\alpha}{\partial\tau} + H(\psi)\left(P_\alpha - \gamma_\alpha\kappa_\alpha\right)|\nabla\phi_\alpha| \\ &+ \frac{H(-\psi)}{\Delta x} S(\psi)\gamma_\alpha\left(\nabla\phi_\alpha\cdot\nabla\psi - \cos\zeta_\alpha|\nabla\phi_\alpha||\nabla\psi|\right) = 0 \ , \\ &\text{where } \alpha = g, o, w. \end{aligned} \tag{16}$$

Here, τ is a fictitious iteration time, P_α is the phase pressure, $\kappa_\alpha = \nabla\cdot(\nabla\phi_\alpha/|\nabla\phi_\alpha|)$ is the scalar curvature field of ϕ_α, $S(\cdot)$ is a sign function, and Δx is the grid spacing.

Equation (16) shows that the evolution equations for the three level set functions ϕ_α, $\alpha = g, o, w$, are uncoupled. This means that the intersection of different level set functions ϕ_α and ϕ_β generally occurs at nonzero contours, which will create overlap or void regions around the $\alpha\beta$ fluid/fluid interfaces. To solve this problem, we update all three ϕ_α by subtracting the average of the two smallest ϕ_α from all ϕ_α in every grid cell after each iteration with equation (16) [51]. This projection step moves the intersections of all ϕ_α to zero contours so that the interfaces between phases α and β are uniquely described by $\phi_\alpha = \phi_\beta = 0$ [39,40]. With the projection step included, equation (16) satisfies Young-Laplace equation (3) in the pore space and Young's equation (4) on the pore walls at equilibrium (that is, when $\partial\phi_\alpha/\partial\tau = 0$ for all $\alpha = g, o, w$).

Fluid phases that are allowed to invade or exit the computational domain are denoted continuous phases and assigned constant phase pressures P_α. However, the MLS method allows for conserving disconnected phase volumes of any selected phases [40]. This is done by calculating phase pressures for all conserved ganglia at the beginning of every iteration step for use in equation (16). The effect of these pressures is to prohibit volume growth or shrinkage of the ganglia in the normal direction along their boundary. For each conserved phase α, the method makes a partitioning of the computational domain Ω that encloses each conserved ganglion of that phase. The pressure of ganglion i of phase α is defined and calculated as [52]:

$$P_{\alpha,i}(\tau) = \frac{V_{\alpha,i}^{(0)} - V_{\alpha,i}^{(\tau)}}{A_{\alpha,i}^{(\tau)}\Delta\tau} \ . \tag{17}$$

Here, $V_{\alpha,i}^{(0)}$ is the initial ganglion volume, while $V_{\alpha,i}^{(\tau)}$ and $A_{\alpha,i}^{(\tau)}$ are the ganglion volume and surface area calculated at every iteration time step τ according to:

$$V_{\alpha,i}^{(\tau)} = \int_{\Omega_{\alpha,i}} H_\epsilon(\psi)H_\epsilon(-\phi_\alpha)dV, \tag{18}$$

and

$$A_{\alpha,i}^{(\tau)} = \int_{\Omega_{\alpha,i}} H_\epsilon(\psi)\delta_\epsilon(\phi_\alpha)|\nabla\phi_\alpha|dV, \tag{19}$$

respectively. Here, $\Omega_{\alpha,i}$ represents the region enclosing domain i of phase α, H_ϵ is a smoothed Heaviside function, δ_ϵ is a smoothed delta function, and $\epsilon = 1.5\times\Delta x$ is the smoothening parameter. Kindly refer to Jettestuen et al. [40] for details on calculations and implementations.

In the MLS method, we approximate normal and advective velocity terms using a weighted essentially non-oscillatory (WENO) scheme with appropriate upwinding techniques, while we approximate area and curvature terms with central differences. The iteration-time discretization uses a third-order Runge-Kutta method with a time step determined from a standard Courant–Friedrichs–Lewy (CFL) condition [53]. Periodically, we reinitialize the level set functions ϕ_α to signed distance functions by solving [53]:

$$\frac{\partial\phi_\alpha}{\partial\tau} + S(\phi_\alpha)(|\nabla\phi_\alpha| - 1) = 0, \tag{20}$$

using the same numerical techniques. For the MLS evolution, convergence occurs when the difference of ϕ_α between the two last reinitializations (denoted by m and n), within a small band (defined by b) around the zero contours in the pore space, is less than a specified tolerance value:

$$\begin{aligned} &\max\left\{\frac{\sum_\Omega H_\epsilon(\psi+\epsilon)H_\epsilon(\phi_\alpha^n+\lambda)H_\epsilon(-\phi_\alpha^n+\lambda)|\phi_\alpha^n-\phi_\alpha^m|}{\sum_\Omega H_\epsilon(\psi+\epsilon)H_\epsilon(\phi_\alpha^n+\lambda)H_\epsilon(-\phi_\alpha^n+\lambda)}\right\} \\ &< c\Delta x \ , \ \text{where } \alpha = g, o, w \ . \end{aligned} \tag{21}$$

Here $\lambda = b\times\epsilon$ is the width of the convergence band. In this work, we use $b = 5$, $c = 0.001$, and a reinitialization interval of 10 MLS iterations.

3.3. Combined model for ripening in three-phase systems

Equations (13) and (14) provide a method to calculate mass transfer between two bubbles separated by a liquid phase, while equations (16) to (19) provide pressure, volume, and surface area for all phases in the system at capillary equilibrium for each physical time step. These sets of equations must be linked together to create the complete model. To this end, we create a list of neighbour pairs such that each element of the pair belongs to a different phase: We use these to generate a list of effective diffusive mass transfer paths (restricted by assumptions (iii) and (iv) in section 3.1) between each pair of bubbles in the system. These mass transfer paths can involve multiple intermediate oil and water regions that link two gas bubbles, so we ensure that each such path is unique. We also calculate the minimum fluid/fluid interfacial area traversed through each path k, denoted $A_{k,\min}$. For example, a path connecting two gas bubbles, *G1* and *G2*, through an intermediate water region, *W*, and an intermediate oil region, *O*, separated by an oil/water interface will consist of three neighbour pairs: bubble 1 and water ($G1.W$), water and oil ($W.O$), and oil and bubble 2 ($O.G2$). So, this path traverses through three interface areas: the gas/water interface area ($A_{G1.W}$), the oil/water interface area ($A_{W.O}$), and the gas/oil interface area ($A_{O.G2}$). Then, $A_{k,\min} = \min(A_{G1.W}, A_{W.O}, A_{O.G2})$.

Here we make two additional assumptions to calculate the phase permeability for each path using equation (14). First, we assume that the mass interaction area in equation (13) can be approximated by $A_{k,\min}$. Second, we assume that the lower phase permeability of J_o and J_w approximates the phase permeability for a mass transfer path containing both oil and water. This second assumption should be adequate in cases where the ratio of high to low phase permeability is very large compared to the distance covered by each liquid on the mass transfer path or when $J_o \approx J_w$. However, we acknowledge that these two assumptions could lead to an overestimation of the equilibrium time in three-phase Ostwald ripening scenarios.

In general, retardation of mass transfer across fluid/fluid interfaces can occur due to the presence of concentration films on either side of the interface, as described by two-film theory and penetration theory [54]. The mass transfer across these films is also diffusive in nature and can contribute as a rate-limiting factor. Such cases require phase permeabilities that incorporate film resistance against the mass transfer at fluid/fluid interfaces to account for the retardation. Likely, this could lead to slower time evolution, yet with insignificant impacts on

the final equilibrium fluid configuration since these film effects act at all fluid/fluid interfaces in the system. Here, we exclude such thin film effects at the interfaces (consistent with other works [e.g., 22,26]) and use the phase permeability of gas in the individual bulk liquids as explained above.

We calculate the mass transfer $\Delta n_{i,k}$ between gas bubbles i and j through a diffusive mass transfer path k for a particular time step Δt [s] by converting equation (13) to a finite difference equation:

$$\Delta n_{i,k} = -J_l A_{k,\min} \times (RT) \left(\ln \frac{f_i}{f_j} \right) \Delta t, \tag{22}$$

where $J_l = J_o$ for oil paths, $J_l = J_w$ for water paths, and $J_l = \min(J_o, J_w)$ for paths containing both oil and water. Mass loss (or gain) for each bubble is calculated by aggregating mass transfers over all the mass transfer paths linking it to other bubbles. After the mass transfer calculations from a time step Δt, the volumes of the gas bubbles are updated to reflect their new mass, and then the MLS method provides the new gas bubble pressures and equilibrium interface positions. We repeat the complete process until the system reaches thermodynamic equilibrium.

In a three-phase scenario, the phase permeability of gas in the two liquids can be vastly different, which requires an adaptive time stepping in equation (22) to accommodate changes that can occur at two different orders of time scales. Here, we limit the time step by setting a threshold for the maximum gas-bubble volume change (for bubbles losing mass), V_{th}/t_{cf}, and fixing the minimum volume of a bubble that is tracked in the simulation, V_{floor}. t_{cf} is a step control factor (set to one initially) that we use to control adaptive time stepping. In this work we use $V_{th} = 10(\Delta x)^2$ and $V_{floor} = 4(\Delta x)^2$ in the presented 2D simulations.

We simulate the ripening as a two-step process, so we carry out two convergence checks: one for the MLS evolution (equation (21)) and another for the complete system. The whole system converges when the maximum pressure difference between all bubbles in the system is lower than a threshold value:

$$\max_i \{P_{g,i}(t)\} - \min_i \{P_{g,i}(t)\} < \varepsilon \ , \tag{23}$$

where ε is an error threshold that we set to $\varepsilon = 5$ Pa in this work. Convergence according to equation (23) will terminate the ripening simulation at a thermodynamic equilibrium state that satisfies equations (6) and (7).

Mass transfer cyclicity is a critical issue that can occur during simulations of ripening [25]. Since our method works on arbitrary pore geometries, we cannot control such mass transfers by *a priori* techniques. Thus, in our model, we continuously check for cyclic mass transfer by looking for a change in mass transfer direction between any two bubbles from the previous to the current time step. Once we detect reversed mass transfer, we increase the control factor t_{cf} alternately by a factor of two and three for each time iteration with cyclic mass transfer. When the cyclicity has disappeared due to the time step reduction, we carry out three additional time iterations using the last determined t_{cf}. If the cyclicity remains absent, we reset the step control factor ($t_{cf} = 1$), or else we continue reducing the time step further to remove the cyclicity. We use a lower bound for the time step to ensure the maximum volume loss of a bubble is at least half a grid-cell volume. Cyclic mass transfer only occurs when the bubble pressures are very close, so its impact is typically minimal. By reducing the time steps, we further decrease this impact until it is negligible. Intuitively, the cyclic mass transfer is related to V_{th}, and a very high threshold can significantly impact the cyclicity observed in the results.

Three-phase scenarios require special handling of mass transfer cyclicity because gas diffusion through oil and water occurs at different time scales. When $J_o > J_w$, mass transfer between gas bubbles in oil may dominate the initial ripening period. In this regime the time step is small, limited by the volume change of a bubble surrounded by diffusion paths through oil. In late stages of the ripening most bubbles in oil are close to equilibrium (that is, their pressure differences are small), while significant mass transfers still occur between bubbles surrounded by water. These bubbles could provide time steps that are larger than in the initial stage because $J_o > J_w$. It is possible that these time steps trigger an increase of a previously negligible cyclicity between bubbles surrounded by oil because the mass transfer through oil is faster. Similar observations can be made for situations where $J_w > J_o$. We manage such scenarios by setting $\Delta n_{i,k} = 0$ in equation (22) for all bubble pairs that satisfy equation (23). This eliminates negligible cyclicity and prevents cyclicity from growing due to the different time scales involved.

The complete model is implemented within the SAMRAI framework that enables parallel simulations and structured adaptive mesh refinement using patch-based data structures [55–57].

4. Results and discussion

We simulate Ostwald ripening of gas bubbles in the presence of oil and water in porous media using a 2D homogeneous and regular pore geometry with dimensions $315\Delta x \times 515\Delta x$ and grid-cell length $\Delta x = 2$ μm. The solid phase consists of circular grains with diameters 165 μm and centers aligned on a square regular network, see Fig. 3(a). The distance between adjacent grain centers is 200 μm. We define a pore as the void space enclosed within a square formed by four neighbouring grain center positions. The volume of a pore is $V_p = 18.6 \times 10^3$ μm^2 (volume in 2D is area), and the total pore space comprises 15 equal pores. In this pore geometry, we study a nitrogen (N_2)-decane-water fluid system where water is the wetting phase, oil (decane) the intermediate-wetting phase, and gas (N_2) the non-wetting phase. A gas bubble located in a pore can start interacting with the pore walls when it is larger in size than the maximal inscribed circle which has volume $0.59V_p$ and radius 58.9 μm. For the simulations we populate the pore geometry with eight gas bubbles of varying size (but with volumes larger than $0.59V_p$) distributed in every other pore in a diagonal pattern, as shown in Fig. 3(a). We use eight bubbles to highlight their individual evolution of pressure and volume in a plot. As an approximation to the effective length of the diffusion paths through liquid, from the interface of one bubble to the interface of its nearest bubble, we use the distance along the medial axis of the pore space between the arcs of two maximal inscribed circles placed in the bubble positions. This length is $\bar{l} = 282$ μm.

The environment pressure and temperature are 15 MPa and 373.15 K. The interfacial tensions for the fluid pairs are $\sigma_{gw} = 53.22 \times 10^{-3}$ Nm^{-1} [48], $\sigma_{go} = 11.5 \times 10^{-3}$ Nm^{-1} [49], and $\sigma_{ow} = 43.65 \times 10^{-3}$ Nm^{-1} [50]. For the decane/water contact angle we use $\theta_{ow} = 40°$, which is within the range reported by Alhosani et al. [34], and then we calculate N_2/water and N_2/decane contact angles to be $\theta_{gw} = 35.7°$ and $\theta_{go} = 31.6°$, respectively, using the relations provided by van Dijke and Sorbie [43] that satisfy equation (5).

Henry's volatility for N_2 in water and oil are $K_w^{px} = 2.08 \times 10^{10}$ Pa [58] and $K_o^{px} = 8.16 \times 10^7$ Pa [59]. The diffusion coefficients for N_2 in the two liquids are $D_w = 6.62 \times 10^{-9}$ m^2 s^{-1} [60] and $D_o = 7.73 \times 10^{-9}$ m^2 s^{-1} [61]. The molar mass M_α and density ρ_α of the three fluids are $M_g = 28.01$ g mol^{-1} and $\rho_g = 128.04$ kg m^{-3}, $M_o = 14.23$ g mol^{-1} and $\rho_o = 677.13$ kg m^{-3}, and $M_w = 18$ g mol^{-1} and $\rho_w = 962.02$ kg m^{-3} [62]. Based on these values the phase permeability of gas (given in equation (14)) in oil and water are $J_o = 1.29 \times 10^{-5}$ mol^2 s kg^{-1} m^{-4} and $J_w = 4.87 \times 10^{-7}$ mol^2 s kg^{-1} m^{-4}.

4.1. Two-phase scenario in porous media

We start by studying Ostwald ripening in a two-phase system where gas bubbles are surrounded by water in the pore space. In the MLS calculations of the interface motion, equation (16), the water behaves as a continuous phase with a prescribed and constant pressure, while we calculate the gas pressure from equation (17) to ensure volume conservation of each bubble.

Fig. 3 shows that the gas bubbles have different volumes and pressures in the initial capillary equilibrium state before ripening. The initial difference in bubble pressure leads to mass transfer between the

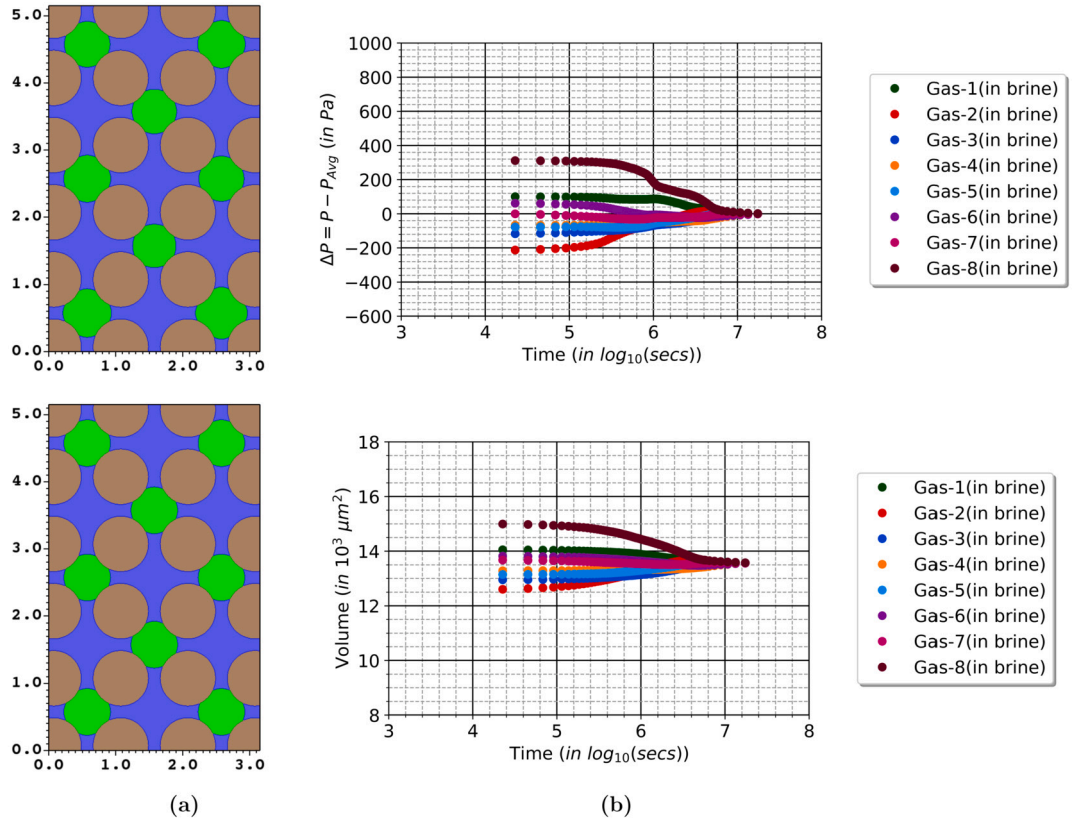

Fig. 3. Ripening of N_2 bubbles surrounded by water in the 2D porous medium. (a) Fluid configurations before (*top*) and after (*bottom*) ripening (gas bubbles are in *green*, water in *blue*, and solid grains in *brown*). The dimensions on the axes refer to the number of grid cells ($\times 10^2$) in each direction. (b) *Top:* Evolution of the difference between bubble pressures and their average pressure over time. *Bottom:* Evolution of bubble volumes over time.

bubbles such that the absolute pressure difference (and hence the chemical potential difference) between all gas bubbles evolves to zero. Since the driving force decreases with evolution, changes in bubble pressures and bubble volumes diminish exponentially with time. The bubbles reach equilibrium at 4.83×10^3 h (≈ 201 days). Note that, when bubbles occupy single pores in this homogeneous medium, the equilibrium condition of equal bubble pressures implies equal bubble volumes [26]. In our simulations the equilibrium bubble volume is approximately 13.57×10^3 μm^2.

In Fig. 3 (b), the pressure evolution of bubble 8 (located at the bottom, right corner of the sample) shows a non-smooth variation compared to the other bubbles. In our model, we assume wetting films on the solid surface do not contribute to diffusive mass transfer, which implies that the mass transfer only occurs between neighbouring bubbles through diffusion paths in bulk liquid regions (see assumption (iii), section 3.1). This makes the ripening evolution of a bubble dependent on the states of its neighbouring bubbles which creates a non-uniform evolution behaviour. Another factor contributing to the evolution of bubble pressures is the non-linear relation between gas/liquid interface curvature (and hence bubble pressure) and bubble volume in the pore geometry. As bubble 8 is the largest in the system, its interfaces are located far into the pore throats. During bubble shrinkage, the curvature change rate increases as the gas/liquid interface retracts from the pore throat, but it starts to decrease before the interface loses contact with the solid surface (and the bubble would redistribute to a circle in the pore).

We have carried out a similar two-phase simulation where oil replaced water, see results in Supplementary information S.1. In this case the range of bubble pressures during the ripening is smaller because $\sigma_{go} < \sigma_{gw}$, and the equilibrium occurs at an earlier time since $J_o < J_w$. In the gas/oil system the equilibrium time is 5.70×10^2 h (≈ 24 days) which is one order of magnitude lower than the time scale for the gas/water system. However, both simulations follow the same general trend and obtain the same equilibrium bubble volume. The contact angles θ_{gw} and θ_{go} are close in values and do not contribute to any significant differences in the fluid configurations.

4.2. Three-phase scenario in porous media

In the three-phase scenarios for gas bubble ripening, we assume the locations of the N_2 bubbles are the same as before, but we distribute the oil and water phases in two halves of the pore space. The initial fluid configuration contains bubbles trapped in oil, bubbles trapped in water, and bubbles trapped between the oil and water. This arrangement yields a foundation to investigate different mass transfer scenarios between a bubble and its set of neighbouring bubbles as their mass transfers occur through diffusion paths containing one and two liquid phases. Further, the mass transfer between two diagonal bubble neighbours occurs through two different paths. To prevent spatial bias, we create four sets of bubble distributions and for each set we also interchange the locations of oil and water, leading to eight distinct initial fluid phase distributions. Here we present simulation results of ripening for two of these fluid configurations where the gas bubble distribution is the same for switched oil and water locations, see Fig. 4 (a) and (b). Supplementary information S.2 presents results for the six other initial fluid distributions as well as tabulated bubble volumes for the initial and final state in each simulation. First, we assume oil and water are continuous phases assigned constant and equal pressures (that is, $P_{ow} = 0$ Pa), while equation (17) determines the gas bubble pressures. We also simulate a scenario where residual oil is trapped in the center of the pore geometry (see Fig. 4 (c)). In this case, we specify the water pressure and calculate the pressures of both the oil ganglion and the gas bubbles with equation (17) to conserve their volumes during MLS evolution.

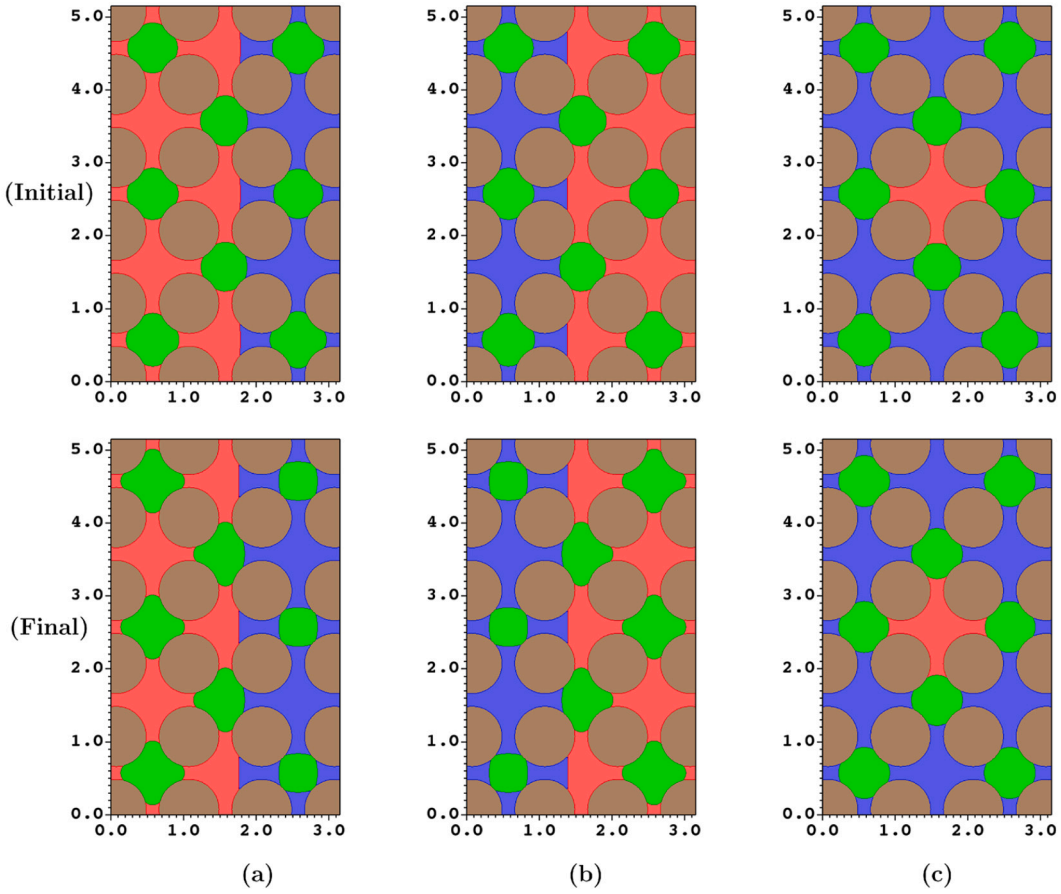

Fig. 4. Fluid configurations before (*top*) and after (*bottom*) ripening of N_2 bubbles in the presence of oil and water in the 2D porous medium (gas bubbles in *green*, oil in red, water in *blue*, and solid grains in *brown*). (a, b) Continuous oil and water at switched locations for the same gas bubble distribution. (c) Trapped oil and continuous water. The dimensions on the axes refer to the number of grid cells ($\times 10^2$) in each direction.

Fig. 5 shows the evolution of bubble pressures and volumes during ripening for the fluid configurations shown in Fig. 4. The evolution times to equilibrium are different in each simulation but they are all of the order 10^3 h. These differences in time are a result of slightly different locations of the interfaces between the bubbles and the liquids in the various fluid configurations, which impacts the bubble pressures and the mass interaction areas $A_{k,\min}$ of the diffusion paths. The bubble evolution in Fig. 5 exhibits several interesting features. Generally, bubbles separated by oil have lower initial pressures than bubbles separated by water because $\sigma_{gw} > \sigma_{go}$. In this homogeneous pore geometry, the interface curvatures of equally sized bubbles separated by oil and water are not vastly different since the contact angles θ_{go} and θ_{gw} are close in values. Scenarios with larger variation in bubble size, or with gas bubbles trapped in more irregular pore geometries, can create less distinct bubble pressure disparities with respect to the surrounding liquid.

Fig. 5 highlights the different time scales for evolution of bubbles in the two liquids that arise because the gas permeability is higher in oil than in water ($J_o > J_w$). First, the bubbles separated by oil equilibrate internally (*local oil regime*), and then this group of bubbles obtains a mutual equilibrium with the other bubbles separated by water (*global water regime*). In the local regime, the dominating mass transfers occur between gas bubbles surrounded by oil, while in the global regime the mass transfers occur between bubbles in oil and bubbles in water, and internally between bubbles in water. The phase permeabilities govern the presence and duration of these distinct regimes: The high permeability (J_o) determines the time scale for equilibration in the local regime while the low permeability (J_w) determines the time scale for achieving thermodynamic equilibrium of the whole system in the global regime. A larger difference in phase permeabilities renders the separation between the two regimes more visible. Finally, Fig. 5 (e) and (f) show that the presence of trapped oil surrounded by gas bubbles reduces the time taken by these bubbles to reach equilibrium internally.

As opposed to the two-phase gas/liquid cases (section 4.1), the three-phase ripening simulations in this homogeneous porous medium show that the equilibrium volumes of the gas bubbles depend on their surrounding liquid. Fig. 5 (b) and (d) show that bubbles surrounded by oil attain the largest size (volume of 16.48×10^3 μm^2), bubbles surrounded by water the smallest size (volume of 9.82×10^3 μm^2), while bubbles surrounded by both liquids attain a medium size (volume of 14.81×10^3 μm^2). In an equilibrium state with equal bubble pressures (and $P_{ow} = 0$ Pa), the distinct bubble sizes in the two liquids must differ to balance the difference in the gas/liquid interfacial tensions. The behaviour of ripening in porous media differs from that in bulk liquid, where all the gas stabilizes in one of the liquids (section 2.1). In bulk liquids, the bubble pressure decreases with increasing bubble size, whereas in porous media, bubble growth (within single pores) leads to increased bubble pressures as the gas/liquid interfaces move towards narrow pore throats. Hence, a gas/oil interface with lower interfacial tension invades farther into a pore throat to maintain the bubble pressure compared with a gas/water interface with higher interfacial tension. In the next section, we investigate how the oil/water capillary pressure impacts this behaviour.

The volume curves in Fig. 5 (b) and (d) also show that the intermediate-sized equilibrium volume attained by the two bubbles surrounded by oil on three sides and water on one side is closer to the volume of bubbles in oil than the volume of bubbles in water. Further, Fig. 5 (f) shows that the equilibrium volume of gas bubbles contacting oil on one side and water on three sides (volume of 13.63×10^3 μm^2)

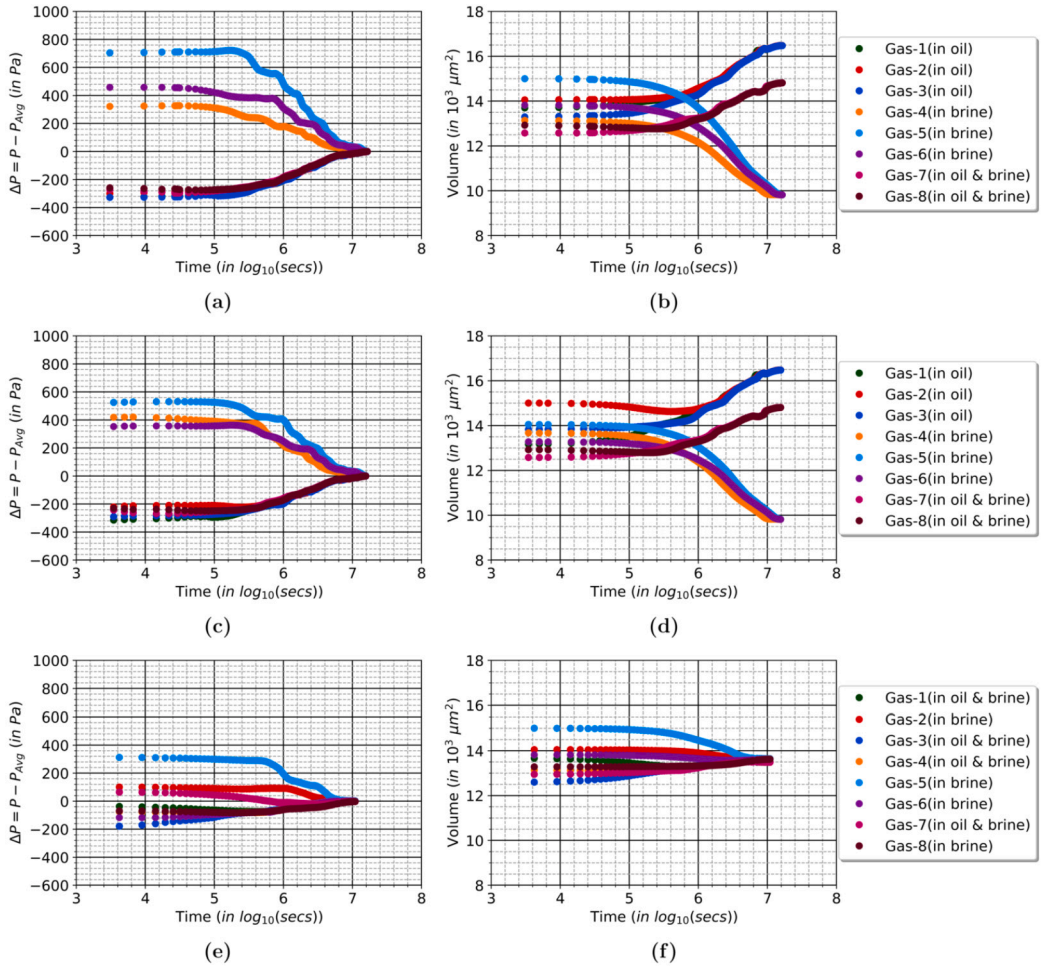

Fig. 5. Evolution of the difference between bubble pressures and their average pressure (*left column*) and evolution of bubble volumes (*right column*) for N_2 bubbles in the presence of oil and water in the 2D porous medium. Simulation results for (a, b) oil on *left* side and water on *right* side of the pore geometry (Fig. 4 (a)), (c, d) water on *left* side and oil on *right* side (Fig. 4 (b)), and (e, f) residual oil trapped in centre of the pore geometry (Fig. 4 (c)).

is barely higher than the volume of the four bubbles surrounded by water (volume of 13.49×10^3 μm^2). From these results we infer that a progressively increasing gas/water interfacial area at the expense of a decreasing gas/oil interfacial area will lower the equilibrium volume of the gas bubbles.

We obtain the same equilibrium volume of gas bubbles in oil and water in Fig. 5 (b) and (d) although the initial gas volumes in the two liquids differ slightly with switched oil and water locations in the pore geometry, see Fig. 4 (a) and (b). A larger porous domain with maintained fractions of gas volume and number of bubbles surrounded by the different liquids will not alter the equilibrium volumes and pressure of the gas bubbles. However, skewed distributions of gas volume fractions in the two liquids will generally give different results that also could involve complete dissolution of some bubbles in one liquid while bubbles in the other liquid could grow beyond the volume of a single pore.

4.3. Impact of oil/water capillary pressure on gas bubble ripening in porous media

Positive oil/water capillary pressure characterizes water-wet reservoirs. Here, we investigate the impact of P_{ow} on gas bubble ripening by conducting simulations for five positive P_{ow} on the same initial fluid configuration used in Fig. 4 (a). In the simulations we specify different but constant phase pressures for oil and water, while we calculate gas-bubble pressures from equation (17). Otherwise, all other simulation parameters are the same as in the last section. Fig. 6 depicts the initial and final configurations from ripening simulations with $P_{ow} = 100$ Pa and $P_{ow} = 1$ kPa. As expected, the oil/water interfaces reside farther into the pore throats for the case with higher P_{ow}; this also impacts the shape of the two gas bubbles in contact with both liquids in the initial capillary equilibrium state.

Fig. 7 shows the pressure and volume evolution of the gas bubbles from the simulations with $P_{ow} = 100$ Pa and $P_{ow} = 1$ kPa. Supplementary information S.3 presents similar results from simulations with $P_{ow} = 200$ Pa, $P_{ow} = 400$ Pa and $P_{ow} = 500$ Pa that underpin the observed trends. For low P_{ow}, pressure differences arise between bubbles in oil and water in the initial state because $\sigma_{gw} > \sigma_{go}$. Higher P_{ow} (obtained by increasing P_o at constant P_w) reduces these pressure differences because the pressures of the bubbles surrounded by oil become higher.

The ripening takes shorter time with increasing P_{ow}. Fig. 7 shows that thermodynamic equilibrium occurs after 3.88×10^3 h (≈ 162 days for $P_{ow} = 100$ Pa) and 1.95×10^3 h (≈ 81 days for $P_{ow} = 1$ kPa). This variance occurs because the final equilibrium volumes of bubbles surrounded by the different liquids also depend on P_{ow}, which leads to smaller total amount of transferred mass during the evolution for higher P_{ow}. As P_{ow} increases, the thermodynamic equilibrium states display a continuously decreasing margin by which bubbles in oil are larger compared to those in water, from 6.67×10^3 μm^2 for $P_{ow} = 0$ (Fig. 5 (b)) to -1.78×10^3 μm^2 for $P_{ow} = 1$ kPa (Fig. 7). Interestingly, at $P_{ow} = 1$ kPa the equilibrium volume for gas bubbles surrounded by water is larger than for gas bubbles surrounded by oil, as opposed to the cases with lower P_{ow}.

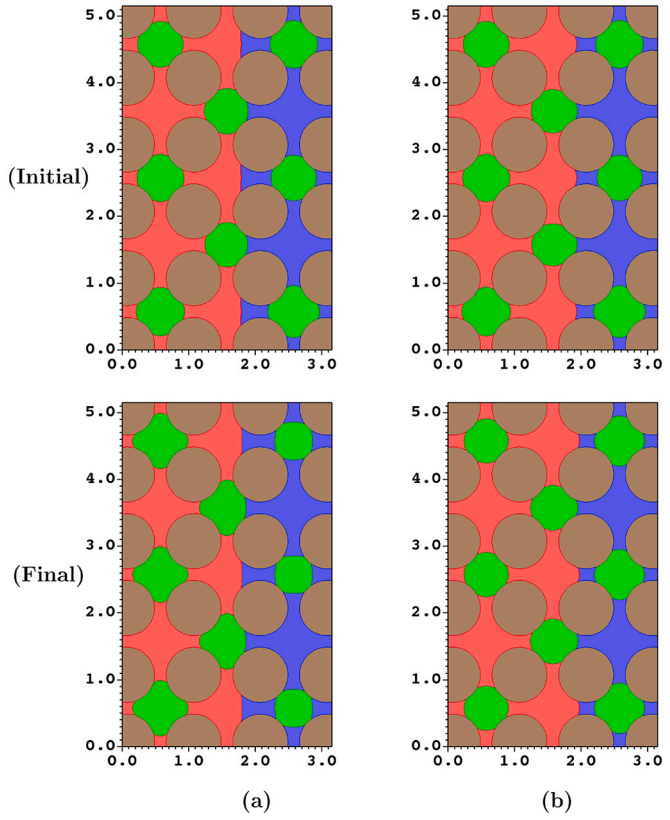

Fig. 6. Configurations before (*top*) and after (*bottom*) ripening of N_2 bubbles in the presence of oil and water in the 2D porous medium for (a) $P_{ow} = 100$ Pa and (b) $P_{ow} = 1$ kPa. Bubbles are in *green*, oil in *red*, water in *blue*, and solid grains in *brown*. The dimensions on the axes refer to the number of grid cells ($\times 10^2$) in each direction.

We highlight this effect in Fig. 8 (a), which shows how the equilibrium volumes for the groups of bubbles surrounded by either or both liquids vary with P_{ow} based on six three-phase simulations (including the case with $P_{ow} = 0$ Pa from Fig. 5 (b)). The equilibrium volumes of gas bubbles with fixed numbers of gas/oil and gas/water interfaces follow distinct, almost linear curves as a function of P_{ow}. The bubble volume in oil decreases, and the bubble volume in water increases with higher P_{ow}. For low P_{ow}, the bubbles in oil are larger than those in water, but at a sufficiently high P_{ow}, the bubbles in water become larger than those in oil. Hence, the response to the raised initial pressure level for bubbles in oil compared to bubbles in water, due to increased oil/water capillary pressure is to reduce the bubble size in oil and increase the bubble size in water at thermodynamic equilibrium. This is also a consequence of the behaviour of bubble expansion in porous media, which leads to higher bubble pressure as narrow pore throats confine the growth. The equilibrium volume of gas bubbles depends on the interfacial tension between gas and surrounding liquids, the fraction of gas/oil and gas/water interface area of the bubbles, and the oil/water capillary pressure. Further work will explore how irregular pore geometries and wetting state impacts these results.

We validate the final states from our simulations using analytic pressure-volume relations previously developed for bubbles in two-phase fluid systems in a similar pore geometry [63]. Here, we adopt this analytic framework to determine simultaneously the two volumes of a gas bubble surrounded by water and a gas bubble surrounded by oil under the constraint of equal gas bubble pressures at prescribed P_{ow}. Supplementary information S.4 describes our solution procedure. With this approach we construct isocurves for constant P_{ow} that describe the relations between the two bubble volumes, see Fig. 8 (b). These curves determine the analytic bubble volumes for the converged bubble pressure in the simulations. We calculate the volume of bubbles in contact with both liquids by comparing the analytic solutions for the bubble volumes surrounded by a single liquid. To evaluate the accuracy of simulated bubble volumes we calculate the root mean square error for each simulation as follows:

$$E_{RMS}[\%] = \sqrt{\sum_{j=w,o,ow} \left(\frac{V_g(j)_{\text{an.}} - V_g(j)_{\text{sim.}}}{V_g(j)_{\text{an.}}} \right)^2} \times 100 \tag{24}$$

where $V_g(j)_{\text{an.}}$ and $V_g(j)_{\text{sim.}}$ are the analytic and simulated volumes of gas bubbles in contact with liquids j. Fig. 8 shows that the simulated results are in good agreement with the analytic results. The highest E_{RMS} is 2.4% which occurs for the simulation with $P_{ow} = 100$ Pa.

5. Conclusions

This work has investigated how the presence of both oil and water impacts Ostwald ripening of gas bubbles in a homogeneous porous medium with identical pores. To this end, we present a numerical model for ripening in three-phase systems that couples the multiphase level set method for capillary-controlled displacement [39,40] with calculations of mass transfer between bubbles to eradicate differences in the chemical potential of the gas component. The method extends the level-set approach for Ostwald ripening in two-phase systems [25] to three-phase fluid configurations where mass transfer between bubbles occurs through oil and water and across oil/water interfaces.

Two-phase simulations show that gas bubbles occupying single pores evolve toward a state of thermodynamic equilibrium where they all have equal volume [26,28]. However, for three-phase fluid systems in homogeneous porous media, our results show that ripening stabilizes gas bubbles in oil to one size and bubbles in water to another size, while bubbles surrounded by both oil and water attain intermediate sizes. The disparity of these bubble volumes depends on the two gas/liquid interfacial tensions, the fractions of bubble interface area with oil and water, and the oil/water capillary pressure. Variation of the initial bubble sizes in the two liquids (for the same total gas volume) does not impact the equilibrium state after ripening.

Bubble volumes in oil decrease, and bubble volumes in water increase as functions of oil/water capillary pressure. Further, bubbles in oil are larger than bubbles in water at low oil/water capillary pressure, whereas for high oil/water capillary pressure it is the opposite. Analytic bubble volume calculations at equilibrium in this pore geometry confirm these trends and validate the numerical results.

The time it takes to reach equilibrium depends on oil/water capillary pressure, phase permeability of gas in the surrounding liquids, and the bubble distribution in the pore geometry. The effect of increasing the oil/water capillary pressure is to reduce the difference in equilibrium size of the bubbles in the two liquids and hence the amount of mass transfer, leading to a shorter evolution time. Higher gas permeability in oil than in water leads to a regime where gas bubbles in oil reach local equilibrium first, followed by a global regime with equilibration of the whole three-phase system.

These findings show a rich ripening behaviour in three-phase systems (even in homogeneous porous media) with striking differences to the ripening behaviour in two-phase systems [22,25,26,28,64]. Three-phase ripening can form larger gas ganglia in one of the liquids. As large ganglia are more prone to gas mobilization, this increases the possibility for gas displacement and reduction of trapped gas saturation in subsurface gas storage applications. Hence, we cannot use two-phase ripening observations to predict residual volume distributions after three-phase ripening.

The findings may have important implications for understanding capillary-gravity equilibrium of gas bubble configurations at the reservoir scale [21,27]. For a migrating gas (or supercritical CO_2) plume in an oil reservoir, our results suggest that, in the oil/water transition zone where oil/water capillary pressure varies with depth, the volume

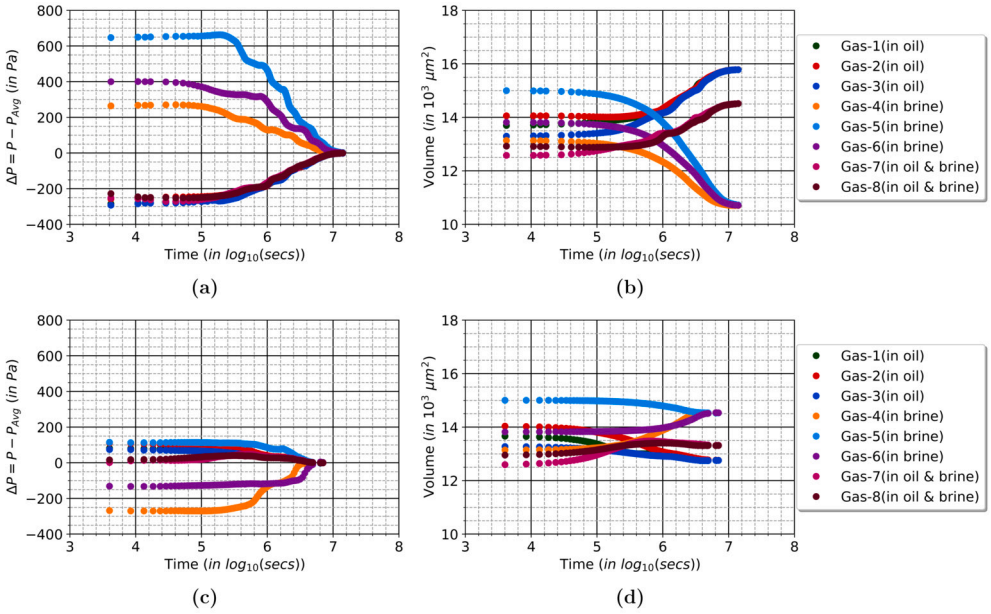

Fig. 7. Evolution of the difference between bubble pressures and their average pressure (*left column*) and evolution of bubble volumes (*right column*) for N_2 bubbles in the presence of oil and water in the 2D porous medium. (a) and (b) $P_{ow} = 100$ Pa, and (c) and (d) $P_{ow} = 1$ kPa.

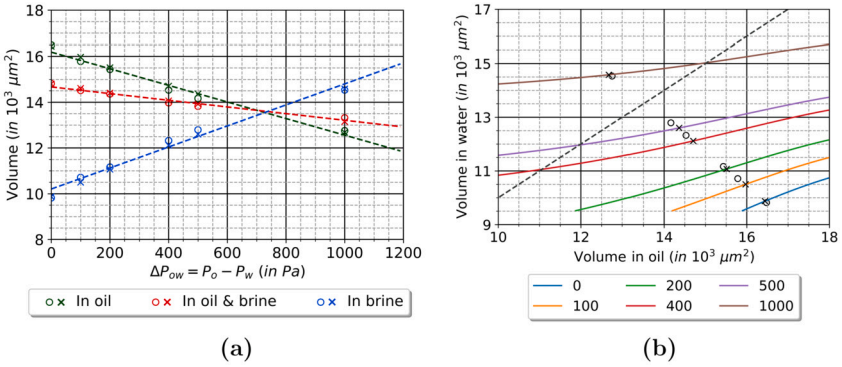

Fig. 8. Relationships between equilibrium volumes of N_2 bubbles after ripening in the presence of oil and water in the 2D porous medium. (a) Bubble volumes as a function of P_{ow} from six simulations (*open circles*), analytic results (*crosses*), and fitted linear curves (*dashed lines*), for bubbles surrounded by oil (*green*), water (*blue*), and both oil and water (*red*). (b) Bubble volume in water as a function of bubble volume in oil for six constant P_{ow} based on analytic solutions constrained by equal bubble pressures (*solid curves*). Data points from the simulated results (*open circles*) and corresponding analytic results (*crosses*) are also shown together with the line that corresponds to equal bubble volumes in oil and water (*dashed line*).

fractions of trapped gas within each of the oil and water phases also vary with depth. Hence, three-phase ripening investigations could potentially provide a basis for developing refined trapping models [65,66], that can differentiate the amount of trapped gas surrounded by the different liquids, for use in reservoir simulation of storage processes.

Although the presented numerical pore-scale model can handle arbitrary pore geometries and fluid configurations, the focus here has been on simulating a nitrogen-decane-water fluid system in an idealized geometry. Future work should investigate three-phase ripening scenarios with skewed initial distributions of gas bubbles trapped within oil and water, where gas ganglia can grow over multiple pores or dissolve completely (as previously explored for two-phase scenarios [25,64]). It is also important to consider heterogeneous media and 3D pore geometries, and to replicate the displacement history in the reservoir as initial condition for the ripening investigations. Microfluidic experiments of three-phase ripening scenarios could also provide input parameters to models and serve model validation.

Finally, gas storage in a subsurface reservoir can occur for a variety of miscibility conditions and wetting states, and future works should assess the impact of these factors on ripening evolution. Two-phase investigations show that the evolution time of ripening depends strongly on the gas type [21,25], while the nature of the gas bubble evolution remains the same [25]. However, in a three-phase scenario, the gas type impacts the gas/liquid interfacial tensions and the wetting behaviour of the three fluids [e.g., 34], in addition to the time scales. Hence for three-phase ripening investigations it is important to use the correct gas under the appropriate reservoir conditions for the gas storage application.

CRediT authorship contribution statement

Deepak Singh: Conceptualization, Data curation, Formal analysis, Investigation, Methodology, Software, Validation, Visualization, Writing – original draft, Writing – review & editing. **Helmer André Friis:** Conceptualization, Data curation, Formal analysis, Investigation, Methodology, Software, Supervision, Validation, Visualization, Writing – original draft, Writing – review & editing. **Espen Jettestuen:** Conceptualization, Data curation, Formal analysis, Investigation, Methodology, Software, Supervision, Validation, Visualization, Writing – original draft, Writing – review & editing. **Johan Olav Helland:** Conceptualization, Data curation, Formal analysis, Funding acquisition, Investigation, Methodology, Project administration, Resources, Software, Supervision,

Validation, Visualization, Writing – original draft, Writing – review & editing.

Declaration of competing interest

The authors declare that they have no known competing financial interests or personal relationships that could have appeared to influence the work reported in this paper.

Data availability

The datasets generated during and/or analysed during the current study are available in the Figshare repository at: https://doi.org/10.6084/m9.figshare.21836859.v1.

Acknowledgement

The financial support was provided by the Research Council of Norway through Petromaks2 project “Foam dynamics in the presence of oil during multiphase flow in porous rock (grant no. 294886)”. The computations were performed on resources provided by UNINETT Sigma2, the National Infrastructure for High Performance Computing and Data Storage in Norway.

Appendix A. Supplementary material

Supplementary material related to this article can be found online at https://doi.org/10.1016/j.jcis.2023.05.070.

References

[1] IEA, World energy outlook 2022, Technical Report, IEA, Paris, 2022, https://www.iea.org/reports/world-energy-outlook-2022.

[2] V. Masson-Delmotte, P. Zhai, H.O. Pörtner, D. Roberts, J. Skea, P. Shukla, A. Pirani, W. Moufouma-Okia, C. Péan, R. Pidcock, S. Connors, J.B.R. Matthews, Y. Chen, X. Zhou, M.I. Gomis, E. Lonnoy, T. Maycock, M. Tignor, T. Waterfield (Eds.), Global Warming of 1.5 °C - an IPCC Special Report on the Impacts of Global Warming of 1.5 °C Above Pre-Industrial Levels and Related Global Greenhouse Gas Emission Pathways, in the Context of Strengthening the Global Response to the Threat of Climate Change, Sustainable Development, and Efforts to Eradicate Poverty, IPCC, 2018.

[3] Z. Jangda, H. Menke, A. Busch, S. Geiger, T. Bultreys, H. Lewis, K. Singh, Pore-scale visualization of hydrogen storage in a sandstone at subsurface pressure and temperature conditions: trapping, dissolution and wettability, J. Colloid Interface Sci. 629 (2023) 316–325, https://doi.org/10.1016/j.jcis.2022.09.082.

[4] B. Pan, X. Yin, Y. Ju, S. Iglauer, Underground hydrogen storage: influencing parameters and future outlook, Adv. Colloid Interface Sci. 294 (2021) 102473, https://doi.org/10.1016/j.cis.2021.102473.

[5] Z. Shi, K. Jessen, T.T. Tsotsis, Impacts of the subsurface storage of natural gas and hydrogen mixtures, Int. J. Hydrog. Energy 45 (2020) 8757–8773, https://doi.org/10.1016/j.ijhydene.2020.01.044.

[6] T. Ajayi, J.S. Gomes, A. Bera, A review of CO2 storage in geological formations emphasizing modeling, monitoring and capacity estimation approaches, Pet. Sci. 16 (2019) 1028–1063, https://doi.org/10.1007/s12182-019-0340-8.

[7] S.K. Al-Mansoori, E. Itsekiri, S. Iglauer, C.H. Pentland, B. Bijeljic, M.J. Blunt, Measurements of non-wetting phase trapping applied to carbon dioxide storage, Int. J. Greenh. Gas Control 4 (2010) 283–288, https://doi.org/10.1016/j.ijggc.2009.09.013.

[8] A.S. Al-Menhali, S. Krevor, Capillary trapping of CO2 in oil reservoirs: observations in a mixed-wet carbonate rock, Environ. Sci. Tehnol. 50 (2016) 2727–2734, https://doi.org/10.1021/acs.est.5b05925.

[9] K. Chaudhary, M.B. Cardenas, W.W. Wolfe, J.A. Maisano, R.A. Ketcham, P.C. Bennett, Pore-scale trapping of supercritical CO2 and the role of grain wettability and shape, Geophys. Res. Lett. 40 (2013) 3878–3882, https://doi.org/10.1002/grl.50658.

[10] S. Krevor, M.J. Blunt, S.M. Benson, C.H. Pentland, C. Reynolds, A. Al-Menhali, B. Niu, Capillary trapping for geologic carbon dioxide storage – from pore scale physics to field scale implications, Int. J. Greenh. Gas Control 40 (2015) 221–237, https://doi.org/10.1016/j.ijggc.2015.04.006.

[11] W. Jia, B. McPherson, F. Pan, Z. Dai, N. Moodie, T. Xiao, Impact of relative permeability and hysteresis models on forecasts of storage associated with CO_2-EOR, Water Resour. Res. 54 (2018) 1109–1126, https://doi.org/10.1002/2017WR021273.

[12] C. Cao, H. Liu, Z. Hou, F. Mehmood, J. Liao, W. Feng, A review of CO_2 storage in view of safety and cost-effectiveness, Energies 13 (2020) 600, https://doi.org/10.3390/en13030600.

[13] S.K. Al-Mansoori, S. Iglauer, C.H. Pentland, M.J. Blunt, Three-phase measurements of oil and gas trapping in sand packs, Adv. Water Resour. 32 (2009) 1535–1542, https://doi.org/10.1016/j.advwatres.2009.07.006.

[14] B. Amaechi, S. Iglauer, C.H. Pentland, B. Bijeljic, M.J. Blunt, An experimental study of three-phase trapping in sand packs, Transp. Porous Media 103 (2014) 421–436, https://doi.org/10.1007/s11242-014-0309-4.

[15] S. Iglauer, A. Paluszny, M.J. Blunt, Simultaneous oil recovery and residual gas storage: a pore-level analysis using in situ X-ray micro-tomography, Fuel 103 (2013) 905–914, https://doi.org/10.1016/j.fuel.2012.06.094.

[16] A.L. Herring, L. Andersson, D. Wildenschild, Enhancing residual trapping of supercritical CO2 via cyclic injections, Geophys. Res. Lett. 43 (2016), https://doi.org/10.1002/2016GL070304.

[17] R. Hu, J. Wan, Y. Kim, T.K. Tokunaga, Wettability impact on supercritical CO2 capillary trapping: pore-scale visualization and quantification, Water Resour. Res. 53 (2017) 6377–6394, https://doi.org/10.1002/2017WR020721.

[18] S. Iglauer, M.A. Fernø, P. Shearing, M.J. Blunt, Comparison of residual oil cluster distribution, morphology and saturation in oil-wet and water-wet sandstone, J. Colloid Interface Sci. 375 (2012) 187–192, https://doi.org/10.1016/j.jcis.2012.02.025.

[19] M. Khishvand, M. Akbarabi, M. Piri, Micro-scale experimental investigation of the effect of flow rate on trapping in sandstone and carbonate rock samples, Adv. Water Resour. 94 (2016) 379–399, https://doi.org/10.1016/j.advwatres.2016.05.012.

[20] L. Zuo, S.M. Benson, Process-dependent residual trapping of CO_2 in sandstone, Geophys. Res. Lett. 41 (2014) 2820–2826, https://doi.org/10.1002/2014GL059653.

[21] M.J. Blunt, Ostwald ripening and gravitational equilibrium: implications for long-term subsurface gas storage, Phys. Rev. E 106 (2022) 045103, https://doi.org/10.1103/physreve.106.045103.

[22] J.A. de Chalendar, C. Garing, S.M. Benson, Pore-scale modelling of Ostwald ripening, J. Fluid Mech. 835 (2017) 363–392, https://doi.org/10.1017/jfm.2017.720.

[23] Y. Li, C. Garing, S.M. Benson, A continuum-scale representation of Ostwald ripening in heterogeneous porous media, J. Fluid Mech. 889 (2020) A14, https://doi.org/10.1017/jfm.2020.53.

[24] Y. Li, F.M. Orr, S.M. Benson, Long-term redistribution of residual gas due to non-convective transport in the aqueous phase, Transp. Porous Media 141 (2021) 231–253, https://doi.org/10.1007/s11242-021-01722-y.

[25] D. Singh, H.A. Friis, E. Jettestuen, J.O. Helland, A level set approach to Ostwald ripening of trapped gas bubbles in porous media, Transp. Porous Media 145 (2022) 441–474, https://doi.org/10.1007/s11242-022-01859-4.

[26] K. Xu, R. Bonnecaze, M. Balhoff, Egalitarianism among bubbles in porous media: an Ostwald ripening derived anticoarsening phenomenon, Phys. Rev. Lett. 119 (2017) 264502, https://doi.org/10.1103/physrevlett.119.264502.

[27] K. Xu, Y. Mehmani, L. Shang, Q. Xiong, Gravity-induced bubble ripening in porous media and its impact on capillary trapping stability, Geophys. Res. Lett. 46 (2019) 13804–13813, https://doi.org/10.1029/2019gl085175.

[28] Y. Mehmani, K. Xu, Pore-network modeling of Ostwald ripening in porous media: how do trapped bubbles equilibrate?, J. Comput. Phys. 457 (2022) 111041, https://doi.org/10.1016/j.jcp.2022.111041.

[29] C. Garing, J.A. de Chalendar, M. Voltolini, J.B. Ajo-Franklin, S.M. Benson, Pore-scale capillary pressure analysis using multi-scale x-ray micromotography, Adv. Water Resour. 104 (2017) 223–241, https://doi.org/10.1016/j.advwatres.2017.04.006.

[30] A.L. Herring, J. Middleton, R. Walsh, A. Kingston, A. Sheppard, Flow rate impacts on capillary pressure and interface curvature of connected and disconnected fluid phases during multiphase flow in sandstone, Adv. Water Resour. 107 (2017) 460–469, https://doi.org/10.1016/j.advwatres.2017.05.011.

[31] P. Øren, W. Pinczewski, Fluid distribution and pore-scale displacement mechanisms in drainage dominated three-phase flow, Transp. Porous Media 20 (1995) 105–133, https://doi.org/10.1007/BF00616927.

[32] A. Scanziani, K. Singh, T. Bultreys, B. Bijeljic, M.J. Blunt, In situ characterization of immiscible three-phase flow at the pore scale for a water-wet carbonate rock, Adv. Water Resour. 121 (2018) 446–455, https://doi.org/10.1016/j.advwatres.2018.09.010.

[33] A. Scanziani, K. Singh, H. Menke, B. Bijeljic, M.J. Blunt, Dynamics of enhanced gas trapping applied to CO_2 storage in the presence of oil using synchrotron X-ray micro tomography, Appl. Energy 259 (2020) 114136, https://doi.org/10.1016/j.apenergy.2019.114136.

[34] A. Alhosani, B. Bijeljic, M.J. Blunt, Pore-scale imaging and analysis of wettability order, trapping and displacement in three-phase flow in porous media with various wettabilities, Transp. Porous Media 140 (2021) 59–84, https://doi.org/10.1007/s11242-021-01595-1.

[35] Z. Qin, M. Arshadi, M. Piri, Micro-scale experimental investigations of multiphase flow in oil-wet carbonates. II. Tertiary gas injection and WAG, Fuel 257 (2019) 116012, https://doi.org/10.1016/j.fuel.2019.116012.

[36] R. Paustian, L. Andersson, J.O. Helland, D. Wildenschild, On the relationship between capillary pressure, saturation, and interfacial area for three-phase flow in water-wet porous media, Adv. Water Resour. 151 (2021) 103905, https://doi.org/10.1016/j.advwatres.2021.103905.

[37] S. Iglauer, T. Rahman, M. Sarmadivaleh, A. Al-Hinai, M.A. Fernø, M. Lebedev, Influence of wettability on residual gas trapping and enhanced oil recovery in three-

phase flow: a pore-scale analysis by use of microcomputed tomography, SPE J. 21 (2016) 1916–1929, https://doi.org/10.2118/179727-PA.
[38] S. Iglauer, A. Paluszny, T. Rahman, Y. Zhang, W. Wülling, M. Lebedev, Residual trapping of CO_2 in an oil-filled, oil-wet sandstone core: results of three-phase pore-scale imaging, Geophys. Res. Lett. 46 (2019) 11146–11154, https://doi.org/10.1029/2019gl083401.
[39] J.O. Helland, J. Pedersen, H.A. Friis, E. Jettestuen, A multiphase level set approach to motion of disconnected fluid ganglia during capillary-dominated three-phase flow in porous media: numerical validation and applications, Chem. Eng. Sci. 203 (2019) 138–162, https://doi.org/10.1016/j.ces.2019.03.060.
[40] E. Jettestuen, H.A. Friis, J.O. Helland, A locally conservative multiphase level set method for capillary-controlled displacements in porous media, J. Comput. Phys. 428 (2021) 109965, https://doi.org/10.1016/j.jcp.2020.109965.
[41] Y. Gao, A. Georgiadis, N. Brussee, A. Coorn, H. van der Linde, J. Dietderich, F.O. Alpak, D. Eriksen, M.M. van den Heuvel, M. Appel, T. Sorop, O.B. Wilson, S. Berg, Capillarity and phase-mobility of a hydrocarbon gas-liquid system, Oil Gas Sci. Technol. (Revue d'IFP Energies nouvelles) 76 (2021) 43, https://doi.org/10.2516/ogst/2021025.
[42] G. Castellan, Physical Chemistry, Addison-Wesley, Reading, Mass, 1983.
[43] M.I.J. van Dijke, K.S. Sorbie, The relation between interfacial tensions and wettability in three-phase systems: consequences for pore occupancy and relative permeability, J. Pet. Sci. Eng. 33 (2002) 39–48, https://doi.org/10.1016/s0920-4105(01)00174-7.
[44] M.I.J. van Dijke, M. Lago, K.S. Sorbie, M. Araujo, Free energy balance for three fluid phases in a capillary of arbitrarily shaped cross-section: capillary entry pressures and layers of the intermediate-wetting phase, J. Colloid Interface Sci. 277 (2004) 184–201, https://doi.org/10.1016/j.jcis.2004.05.021.
[45] M.I.J. van Dijke, M. Piri, J.O. Helland, K.S. Sorbie, M.J. Blunt, S.M. Skjæveland, Criteria for three-fluid configurations including layers in a pore with nonuniform wettability, Water Resour. Res. 43 (2007) W12S05, https://doi.org/10.1029/2006WR005761.
[46] Y. Zhou, J.O. Helland, D. Hatzignatiou, Computation of three-phase capillary entry pressures and arc menisci configurations in pore geometries from 2D rock images: a combinatorial approach, Adv. Water Resour. 69 (2014) 49–64, https://doi.org/10.1016/j.advwatres.2014.03.006.
[47] P. Stevenson, Inter-bubble gas diffusion in liquid foam, Curr. Opin. Colloid Interface Sci. 15 (2010) 374–381, https://doi.org/10.1016/j.cocis.2010.05.010.
[48] G. Wiegand, E.U. Franck, Interfacial tension between water and non-polar fluids up to 473 K and 2800 bar, Ber. Bunsenges. Phys. Chem. 98 (1994) 809–817, https://doi.org/10.1002/bbpc.19940980608.
[49] Z. Pan, J.P.M. Trusler, Interfacial tensions of systems comprising N_2, 7 mass% KI (aq), decane and iododecane at elevated pressures and temperatures, Fluid Phase Equilib. 556 (2022) 113364, https://doi.org/10.1016/j.fluid.2021.113364.
[50] A. Georgiadis, G. Maitland, J.P.M. Trusler, A. Bismarck, Interfacial tension measurements of the (H_2O + n-decane + CO_2) ternary system at elevated pressures and temperatures, J. Chem. Eng. Data 56 (2011) 4900–4908, https://doi.org/10.1021/je200825j.
[51] F. Losasso, T. Shinar, A. Selle, R. Fedkiw, Multiple interacting liquids, ACM Trans. Graph. 25 (2006) 812–819, https://doi.org/10.1145/1141911.1141960.
[52] R.I. Saye, J.A. Sethian, The Voronoi implicit interface method for computing multiphase physics, Proc. Natl. Acad. Sci. 108 (2011) 19498–19503, https://doi.org/10.1073/pnas.1111557108.
[53] S. Osher, R. Fedkiw, Level Set Methods and Dynamic Implicit Surfaces, Springer, New York, 2003.
[54] K.G. Clarke, Bioprocess Engineering - An Introductory Engineering and Life Science Approach, Woodhead Publishing Limited, 2013, pp. 147–170.
[55] R.W. Anderson, W.J. Arrighi, N.S. Elliott, B.T. Gunney, R.D. Hornung, SAMRAI Concepts and Software Design, Technical Report LLNL-SM-617092-DRAFT, Livermore, CA, 2013.
[56] R.D. Hornung, S.R. Kohn, Managing application complexity in the SAMRAI object-oriented framework, Concurr. Comput., Pract. Exp. 14 (2002) 347–368, https://doi.org/10.1002/cpe.652.
[57] R.D. Hornung, A.M. Wissink, S.R. Kohn, Managing complex data and geometry in parallel structured AMR applications, Eng. Comput. 22 (2006) 181–195, https://doi.org/10.1007/s00366-006-0038-6.
[58] R. Sander, Compilation of Henry's law constants (version 4.0) for water as solvent, Atmos. Chem. Phys. 15 (2015) 4399–4981, https://doi.org/10.5194/acp-15-4399-2015.
[59] J. Tong, W. Gao, R.L. Robinson, K.A.M. Gasem, Solubilities of nitrogen in heavy normal paraffins from 323 to 423 K at pressures to 18.0 MPa, J. Chem. Eng. Data 44 (1999) 784–787, https://doi.org/10.1021/je980279n.
[60] S.P. Cadogan, G.C. Maitland, J.P.M. Trusler, Diffusion coefficients of CO_2 and N_2 in water at temperatures between 298.15 K and 423.15 K at pressures up to 45 MPa, J. Chem. Eng. Data 59 (2014) 519–525, https://doi.org/10.1021/je401008s.
[61] J.L. Rivera, J. Alejandre, Transport properties of nitrogen and n-alkane binary mixtures, Fluid Phase Equilib. 185 (2001) 389–396, https://doi.org/10.1016/s0378-3812(01)00486-1.
[62] E.W. Lemmon, I.H. Bell, M.L. Huber, M.O. McLinden, NIST Chemistry WebBook, NIST Standard Reference Database Number 69, National Institute of Standards and Technology, 1997, https://doi.org/10.18434/T4D303, retrieved October 19, 2022.
[63] C. Wang, Y. Mehmani, K. Xu, Capillary equilibrium of bubbles in porous media, Proc. Natl. Acad. Sci. USA 118 (2021) e2024069118, https://doi.org/10.1073/pnas.2024069118.
[64] Y. Mehmani, K. Xu, Capillary equilibration of trapped ganglia in porous media: a pore-network modeling approach, Adv. Water Resour. 166 (2022) 104223, https://doi.org/10.1016/j.advwatres.2022.104223.
[65] C.S. Land, Calculation of imbibition relative permeability for two- and three-phase flow from rock properties, SPE J. 8 (2008) 149–156, https://doi.org/10.2118/1942-PA.
[66] E.J. Spiteri, R. Juanes, M.J. Blunt, F.M. Orr, A new model of trapping and relative permeability hysteresis for all wettability characteristics, SPE J. 13 (2008) 277–288, https://doi.org/10.2118/96448-PA.